Wind tunnel demonstration of galloping mitigation with a purely nonlinear energy sink

Michael M. Selwanis[a,b,*], Guilherme Rosa Franzini[c], Cédric Béguin[a] and Frédérick P. Gosselin[a,**]

[a]Department of Mechanical Engineering, Polytechnique Montréal , Québec, Canada
[b]Aerospace Engineering Department, Military Technical College, Cairo, Egypt
[c]Offshore Mechanics Laboratory, Escola Politécnica, University of São Paulo, Brazil

ARTICLE INFO

Keywords:
Non-linear energy sink
Vibration suppression
Square prism
Galloping
Energy transfer
Wind tunnel tests

ABSTRACT

Galloping is a critical type of flow-induced vibration (FIV) arising on power transmission lines, high rise buildings, pipe and cables bundles in the oil and gas industry. In this paper, we present a purely nonlinear energy sink (NES) that mitigates the galloping of a square prism. The NES is composed of a ball rotating freely in a circular track attached to the prism. The ball's dynamics is coupled to that of the prism in a purely nonlinear way by inertia. We experimentally assess how this simple NES reduces the prism vibration by comparing the prism amplitude responses with and without the NES. A supplementary video presents these experiments, during which the NES ball exhibits different dynamics in three regimes; oscillatory, intermittent, and rotational. We characterise the ball behaviour and its effect on the prism response in each regime. The oscillatory regime appears at low flow speeds at which both the prism and the ball oscillate with small amplitude. The intermittent regime represents a transition mode within a small range of flow speeds and corresponds to a small jump in the vibration amplitude of the prism. The rotational regime appears at higher flow speeds, where the ball oscillates with relatively high angular speeds resulting in a strong modulated response of the prism. The design of the NES allows to easily vary its track dimensions to use a ball of different sizes and masses. Accordingly, we demonstrate the influence of the main NES parameters, which are the ball mass, NES track radius, ball friction, and radial clearance between NES track walls and the rotating ball, on both the prism response and the ball behaviour. The NES we present is directly amenable to mitigate other types of FIV.

1. Introduction

Transverse galloping is a critical type of flow-induced vibration (FIV) that commonly occurs at high flow speeds. During heavy wind, galloping may have destructive effects on many structures such as skyscrapers, transmission lines, and road signs. A linear Tuned Mass Damper (TMD) is a simple device used for damping vibration of structures. This mass-spring-damper system (Hijmissen and van Horssen, 2007) is tuned to change the natural frequency of the system. A TMD works efficiently in a narrow frequency band but adds new potential resonances to the main structure. Contrary to the TMD, another particular class of suppressors known as nonlinear energy sinks (NES) have no linear natural frequency (Lee et al., 2008) and can engage with the primary vibrating systems over a broad range of frequencies reducing its vibration amplitude.

A NES is a passive vibration suppressor that consists of a mass added to a primary structure and characterized by a non-linearizable stiffness and usually linear damping properties (Lee et al., 2008). A NES without direct attachment to the primary structure (Pennisi et al., 2017; Li et al., 2018) is a special type of such devices with zero-stiffness, their dynamics is purely nonlinear. A NES works by Targeted Energy Transfer (TET) (Vakakis et al., 2008; Gendelman, 2008): during vibration, a portion of the energy is transferred irreversibly from the primary structure to the NES reducing vibration amplitudes.

The great interest in the field of nonlinear energy absorption has led to various NES designs. In a vibro-impact NES, the impacts of balls with rigid walls dissipate energy (Gendelman and Alloni, 2015). In a translative NES, a small mass attached to the main structure by an essentially non-linear spring and a dashpot absorbs vibration during its

*Corresponding author; email address (michael.selwanis@polymtl.ca)
**Principal corresponding author; email address (frederick.gosselin@polymtl.ca)
ORCID(s):

Nomenclature

δ	Logarithmic decrement, $= 2\pi\zeta_y$ for lightly damped systems
μ	Radial clearance between the NES ball and the track side walls, $= w_t - 2\,r_b$
ω	Natural angular frequency, $= \sqrt{k/m}$
θ	Ball angular coordinates relative to the prism
A	Vibration amplitude
c	System damping coefficient
c_θ	Ball damping coefficient
D	Side length of the square prism cross section
f_n	Natural frequency, $= \omega/2\pi$
f_{vs}	Vortex shedding frequency
k	Spring stiffness
L	Height of the square prism
M	Total oscillating mass
m_b	NES ball mass
r	NES track mean radius
r_b	NES ball radius
S_t	Strouhal number
t	time
U	Flow stream velocity
U_r	Reduced flow velocity, $= U/\omega D$
U_c	Critical flow speed
$U_{lock-in}$	Lock-in flow speed, $= f_{vs}D/S_t$
w_t	NES track width
y	Displacement normal to the flow direction
Non-dimensional parameters	
$\hat{\mu}$	NES relative clearance, $= \mu/r_b$
$\hat{A}$	Non-dimensional vibration amplitude, $= A/D$
$\hat{m}$	NES mass ratio, $= m_b/M+m_b$
$\hat{r}$	NES radius ratio, $= r/D$
$\hat{Y}$	Non-dimensional vibration displacement, $= y/D$
Λ	Onset velocity ratio, $= U_g/U_{vs}$
ζ_θ	Ball damping ratio, $= c_\theta/2m_b r^2\,\omega$
ζ_y	System damping ratio, $= c/2\,(M+m_b)\,\omega$

translational motion (Dongyang et al., 2018; Guo et al., 2017). While in a rotative NES (Saeed et al., 2019), a rotating rigid bar with a tip-mass attached to the main structure represents another technique for vibration suppression. The rotative NES is a simple and promising device that can damp vibration without a spring element (Ueno and Franzini, 2019).

Only a few contributions are concerned with the passive suppression of galloping by a NES. Dai et al. (2016) analytically and numerically studied the response of a square prism fitted with a translative NES. This study pointed out the influence of the NES parameters on the onset of the critical galloping velocity, as well as the strongly modulated responses of the prism. Teixeira et al. (2018) addressed a similar problem with considering a rotative NES. Throughout the numerical simulations, the NES can reduce the vibration amplitudes of the prism to half its original values.

However, in the last decade, researchers have used various NES designs to suppress a particular type of FIV different from galopping, e.g., vortex-induced vibrations (VIV). Tumkur et al. (2013) investigated the dynamics of a cylinder fitted with a translative NES using Computational Fluids Dynamics (CFD) and reported a 75 % reduction in the cylinder vibration amplitudes due to vortex shedding. A similar approach was employed by Mehmood et al. (2014), who pointed out the dependence of the suppression efficiency with the initial conditions. Blanchard et al. (2020) focused on VIV suppression using a rotative NES. The authors used CFD approaches for computing the fluid loads and highlighted the significant energy transfer that appears in the strongly modulated responses of the cylinder. Conversely, Dai et al. (2017) employed the wake-oscillator models for evaluating the fluid forces due to VIV and showed that a translative NES can similarly modulate the cylinder responses. Ueno and Franzini (2019) studied the effect of the NES parameters on the oscillation amplitude of the cylinder.

Experimental investigations related to NESs are fewer than theoretical ones and mostly deal with the NES as a passive suppressor for building vibration. Wierschem et al. (2012) tested a 2-DOF NES to damp impulsive excitation showing a good effect for TET on improving the structural damping. In a similar study (AL-Shudeifat et al., 2013), a vibro-impact NES highly enhanced the damping properties of a structure. Wang et al. (2016) examined a different vibro-impact NES showing its effect on mitigating impulsive and seismic excitation. Wierschem et al. (2017) used a system of NESs to reduce the structural vibrations generated from transient loads due to blast testing of a large scale steel structure.

In terms of mitigating FIV with a NES, few experiments are available in the literature. Dongyang et al. (2018); Dai

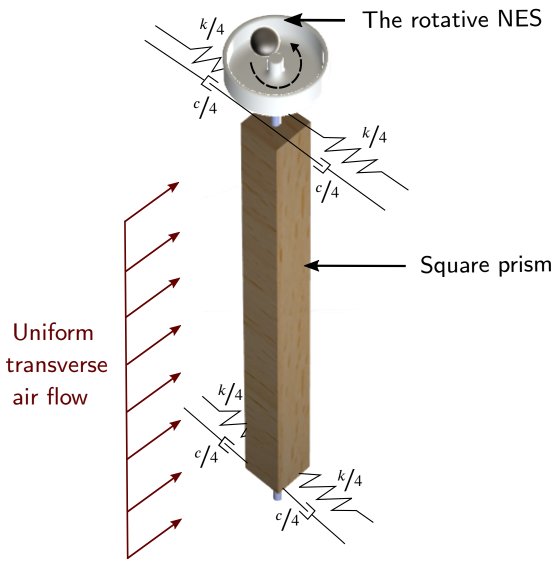

Figure 1: Schematic drawing of the square prism model with the rotative NES.

et al. (2017) performed experiments only to validate the VIV model of the cylinder. Despite a number of theoretical studies concerning various NES designs, few experimental demonstrations are available and even fewer industrial applications are reported. This is possibly due to the practical difficulties of implementing complex NES designs with cams, springs and other moving structures.

The automatic ball balancer (ABB) (Makram et al., 2017) is a different type of passive devices used for the reduction of rotor vibration generated from system imbalance. An ABB consists of metal balls rotating freely in a circular track due to dynamic interaction with rotor vibration (Majewski et al., 2015). The balls are required to reach a certain position to counteract the system imbalance then stop relative to the rotor. The simplicity of such balancers has extended their use to some applications such as optical disc drives (Lu and Hung, 2008) and washing machines (Chen et al., 2015). However, the concept of ABB is different from a rotative NES that depends on energy dissipation to damp the vibrating structure. Whereas ABBs are fabricated with minimal friction to allow the balls to counter the rotary imbalance, a rotative NES requires dissipative forces for damping. Nevertheless, the simplicity and robustness of the ABB is highly inspiring for the design of a rotative NES.

This paper experimentally demonstrates the mitigation of the galloping of a square prism due to the dynamic interaction with a purely NES. We use a ball free to roll in a circular track as a simple NES without direct attachment to the primary system. The paper is structured in four sections. Following this introduction, section 2 presents the experimental arrangement and the model description. Section 3 presents the results in three parts: the influence of the proposed NES on reducing the galloping amplitude, the different dynamical regimes, and the effect of the main NES parameters on its behaviour and the prism galloping response. Finally, section 4 brings the conclusion. In the supplementary information, we provide a video succinctly presenting the experimental setup and highlighting the article's main conclusion.

2. Methodology

We performed the experiments in the closed-loop wind tunnel (Model 407-B, ELD, Lake City, MN, USA) of the mechanical engineering department of Polytechnique Montréal. The wind tunnel test section is $60 \times 60\,\mathrm{cm}^2$ and the maximum air speed produced is 90 m/s.

2.1. Model description

The schematic drawing of our model (Fig. 2) shows a square prism of side length D mounted on two identical supports of equivalent stiffness k, and a damping coefficient c. The prism can only vibrate transversely, with displacement

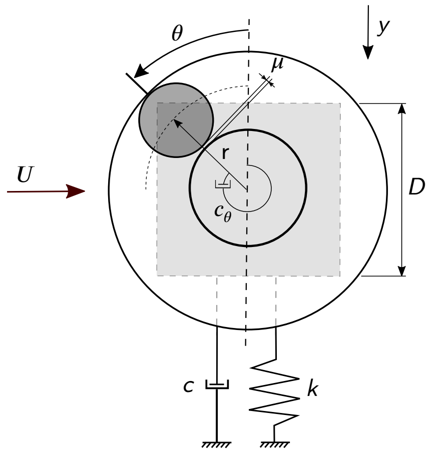

Figure 2: Schematic drawing of the square prism with the rotative NES.

y, to a free stream of velocity U, resulting in automatic rotation of the NES ball in a circular track of mean radius r. The ball angular displacement θ is positive counter-clockwise. A ball damping coefficient c_θ affects the ball rotation due to friction and air resistance. The ball moves on a horizontal plane. Hence, its motion is not affected by the gravitational acceleration.

We designed a lightweight prism spanning almost the entire height of the wind tunnel test section without too much blockage effect. Fig. 3(a) presents the square prism model of 5 cm side length and 58 cm height made of balsa wood and covered with a vinyl smooth. The prism blocks 8.1% of the test section area. Two end plates (2) made of light Formica with 33 cm length, 13 cm width, and 0.1 cm thickness installed at the two ends of the square prism prevent air from escaping the wind tunnel test section. Another pair of smaller plates (3) of 15 cm length and 14 cm width are installed 8 cm away from each end. These inner plates help approach two-dimensional flow conditions; see Bearman et al. (1987). The square prism is mounted onto two identical elastic supports allowing cross-wise oscillations. Each support consists of two leaf springs (4) as shown in Fig. 3(b). The length of the leaf springs is long compared to the maximum allowed vibration amplitude. Therefore, the square prism is assumed to behave as a single degree of freedom (DOF) system vibrating transversely to the flow. Free vibration tests allowed evaluating the equivalent total oscillating mass $M = 1.39$ kg , the natural frequency $f_n = {}^{\omega}/_{2\pi} = 2.56 \pm 0.01$ Hz and structural damping ratio $\zeta_y = {}^{\delta}/_{2\pi} = 0.01$. In our experiments, the prism transverse vibration is restricted by the slot length of 15 cm in the top and bottom boards of the wind tunnel test section, which allows a maximum amplitude A of 7.5 cm (equal to 1.5 times the square prism side length). We only tested one mass ratio for the prism and cannot infer about other mass ratios that can be a question of future work, notably modelling work.

Table 1
Physical parameters of the experiment.

Cross-section side length, D	5 cm
Prism length, L	58 cm
Equivalent stiffness, k	360 N/m
Total oscillating mass, M	1.39 kg
Natural frequency, f_n	2.56 Hz
Structural damping ratio, ζ_y	0.01
Critical flow speed, U_c	6.5 m/s
The lock-in flow speed, $U_{lock-in} = {}^{f_{vs}D}/_{S_t}$	0.96 m/s
Onset velocity ratio, $\Lambda = {}^{U_c}/_{U_{lock-in}}$	6.8
Reduced flow velocity, $U_r = {}^{U}/_{\omega D}$	2.6 - 28.5

This paper provides parametric study on the effect of main NES parameters in the non-dimensional form for easier generalization. Consequently, we define the following dimensionless parameters: the non-dimensional vibration dis-

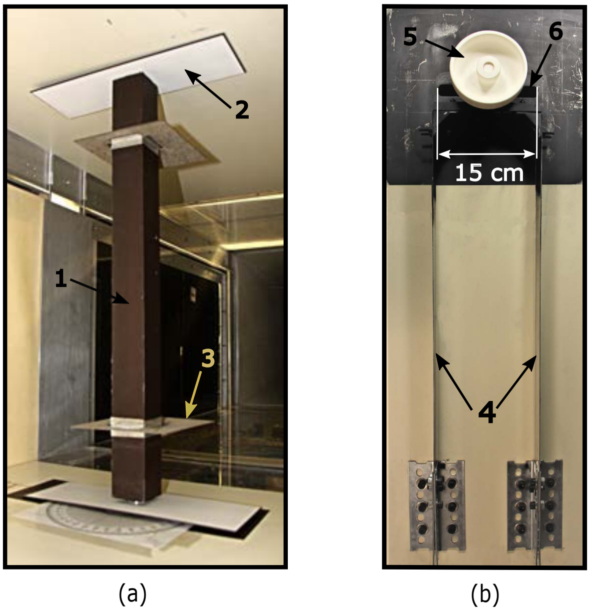

Figure 3: Experimental set-up showing (a) the model inside the wind tunnel test section and (b) the test section top view. The main components are numbered: (1) the manufactured square prism, (2) outer plates, (3) inner plates, (4) the support that mainly consists of two leaf springs, (5) the NES main body attached to the upper end of the square prism, (6) a slot of 15 cm length.

placement $\hat{Y}$ and amplitude $\hat{A}$; the reduced velocity U_r; the NES mass ratio $\hat{m}$ and radius ratio $\hat{r}$; and the relative radial clearance $\hat{\mu}$ that relates the radial clearance μ between the NES track walls and the ball to the ball radius r_b:

$$\hat{Y} = \frac{y}{D}, \quad \hat{A} = \frac{A}{D}, \quad U_r = \frac{U}{\omega D}, \quad \hat{m} = \frac{m_b}{(M + m_b)}, \quad \hat{r} = \frac{r}{D}, \quad \hat{\mu} = \frac{\mu}{r_b}. \tag{1}$$

2.2. NES design and fabrication

We propose a simple NES design (Fig. 4) consisting of the main body (1), various size bushings (2), steel balls (3), and a lubricating fluid (4). We built the NES to be about the size of the prism dimension and made it as light as possible. A 3D printer (Ultimaker3, Ultimaker) printed the NES components with white Poly-Lactic Acid (PLA) plastic. This modular design aims to easily vary the main NES parameters by swapping some parts. Bushings of various sizes allow varying the racetrack inner and outer radii. Lubrication of the NES track decreases the friction between the rotating ball and the NES body, thus changes the ball damping.

2.3. Measuring system

A high-speed Camera (Motion BLITZ Cube 4, MIKROTRON) captured the motion of both the prism and the NES ball with a resolution of 0.085 mm to allow for post-treatment image analysis. The memory of the high-speed camera and the frame dimensions limit the recording time to 40 seconds. A MATLAB code was written to process the recorded image series and plot the prism vibrating displacement y and the ball angular displacement θ with time t. To ensure a steady-state, three minutes elapsed each time between setting the new wind tunnel flow speed and starting the camera recording. We repeated the measurement for incrementing flow speed with increasing values to plot the prism maximum amplitude A (max abs y(t)) *versus* flow speed U demonstrating the system response.

3. Results

We present the results of this study in three parts: the NES effect on mitigating the galloping of the square prism; the different dynamical regimes experienced by the NES; and a parametric study on the NES parameters.

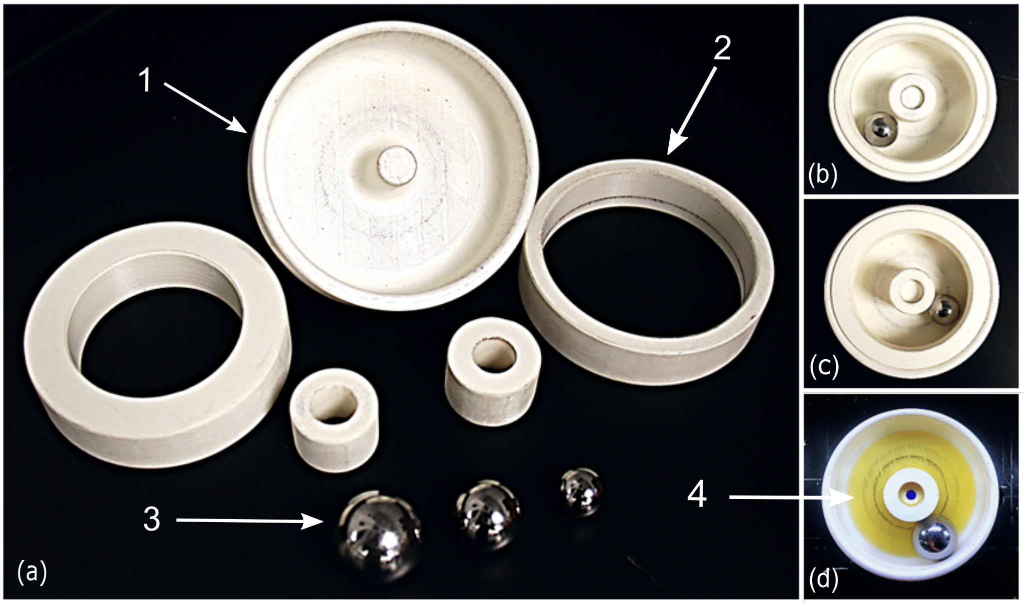

Figure 4: (a) Exploded view for NES parts: 1- NES main body, 2- various size bushings, 3- steel balls, and 4- a lubricating fluid. (b), (c) and (d) NESs with varing the track dimensions.

3.1. NES Effect on the Prism Response

We recorded the dynamics of the prism without NES for incrementing flow speed. To clarify the nature of the vibrations, we compare the critical velocity measured for galloping versus the expected lock-in velocity for VIV. We define a critical flow speed U_c at which the prism starts to gallop exceeding 4 mm amplitude. This speed is observed experimentally as 6.5 m/s. Considering a Strouhal number S_t of 0.133 for a square prism (Bearman et al., 1987), the lock-in flow speed of our model $U_{lock-in} = {}^{f_{vs}D}/_{S_t} = 0.96$ m/s. Hence, the onset velocity ratio, $\Lambda = {}^{U_c}/_{U_{lock-in}} = 6.8$ (table 1), and the square prism response without the NES shows a pure galloping with minimal interaction with vortex shedding. We repeated the measurement with a NES of mass ratio $\hat{m} = 0.08$, and a radius ratio $\hat{r} = 0.6$. In this subsection, the measured data is presented in dimensional form without any post-treatment.

Fig. 5 compares the maximum vibration amplitudes of the prism with and without the NES at different flow speeds. Beyond the critical speed U_c, the prism galloping amplitude dramatically increases with the flow speed to exceed the limit of our experiment 75 mm at a flow speed of 12.7 m/s. The prism response with the NES, presented in Fig. 5 by the dashed line, shows a significant decrease in vibration amplitude. The NES maintains the prism vibration displacements below 5 mm up to a flow speed of 11.2 m/s. With increasing flow speed, a little jump in the vibration amplitude occurs at a flow speed of 12.7 m/s. Then, the amplitude of the prism with the NES plateaus until a flow speed of 20.2 m/s. In this flow speed range, the vibration amplitude does not exceed 30 mm. Above this flow speed, the NES is ineffective and unable to keep the prism vibration below the maximum allowed amplitude. The NES increases the flow speed at which the prim galloping amplitude reaches the limit of our experiment from 12.7 to 21.7 m/s.

Figs. 6(a-c) present the amplitude spectra obtained from the Fast Fourier Transform (FFT) of the vibrating prism displacement in semi-log scale at different flow speeds 9.7, 11.2 and 12.7 m/s. Figs. 5(a) and (b) compare the frequency response of the prism with and without the NES. The NES has no significant effect on the natural frequency of the prism $f_n = 2.56$ Hz even at higher flow speed $U = 12.7$ m/s where the ball rotates achieving complete revolutions.

We can observe that the NES engages with the system dynamics resulting in the transfer of energy from the vibrating prism to the NES in the form of ball rotation kinetic energy. Hence, the NES delays galloping occurrence and significantly mitigates the prism amplitudes for flow speeds between 9.7 m/s and 20.2 m/s. This range of flow speeds can be referred to as the NES effective range. At higher flow speeds, the galloping of the prism increases and the prism energy is too high to be absorbed by the NES. One of the main advantages of the NES is that it does not change the characteristics of the primary system contrary to other vibration absorbers of linear stiffness.

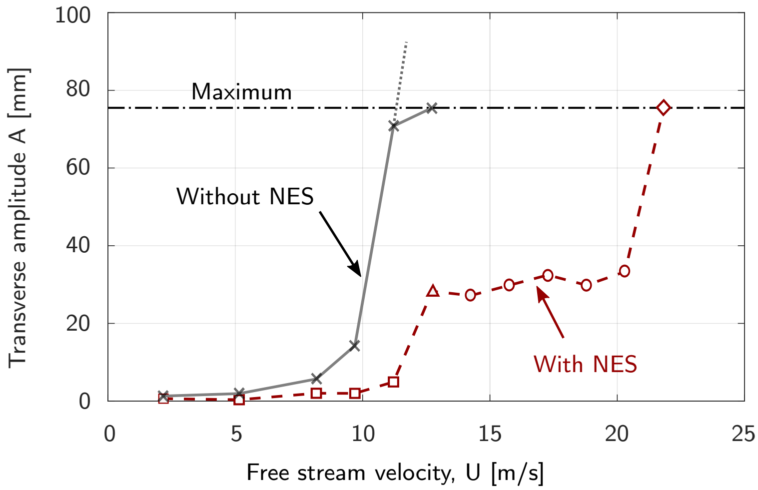

Figure 5: The prism responses with and without the NES of mass ratio $\hat{m}$=0.08, and a radius ratio $\hat{r}$=0.6, showing the oscillatory regime □, the intermittent regime △, and the rotational regime ○.

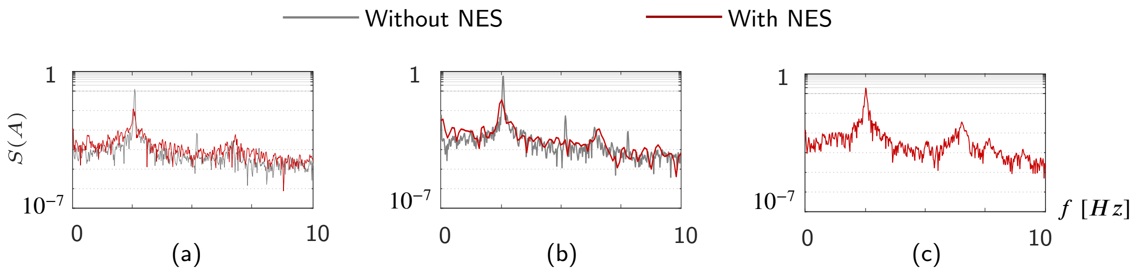

Figure 6: The amplitude spectrum of the vibrating prism with NES (red curve) at different flow speeds U =: (a) 9.7 m/s; (b) 11.2 m/s; (c) 12.7 m/s. The amplitude spectrum of the vibrating prism without NES (gray curve) is shown only in (a) and (b).

3.2. Different NES Dynamics

We demonstrate the different NES dynamics from the time history of the NES ball angular displacement and its effect on the prism response at different flow speeds. The NES experiences three different response modes; oscillatory, intermittent, and rotational. Fig. 7 shows the time histories of the prism displacements and the ball angular displacements at nine flow speeds U between 9 and 20.2 m/s. For the three lower speeds, Figs. 7 (a-c) present both the dynamics with and without NES. For Figs. 7 (d-i), $U \geq 12.7$ m/s, the prism without NES reaches the maximum allowed amplitude of the setup. The behaviour of the NES and its impact on the dynamics of the prism can be broken down into three regimes, which we named according to the ball behaviour.

The *oscillatory regime* is shown in Figs. 7 (a-c), where the NES ball angular displacement does not exceed 75^o. However, it reduces the prism galloping amplitude. Fig. 7 (c) shows a significant reduction in the maximum amplitude by the NES from 70 mm to 5 mm at a flow speed U = 11.2 m/s.

The *intermittent regime*, shown in Fig. 7 (d), appears as a transition between two different regimes in a small range of flow speeds. The ball rotates with relatively low angular speed keeping the prism vibration amplitude below 28 mm. This regime is characterized by a nearly steady vibration for the prism and a ball rotation of a small number of successive complete revolutions not exceeding five revolutions.

The *rotational regime* appears in a higher range of flow speeds from 14.2 to 20.2 m/s, as shown in Figs. 7 (e-i). The prism shows a strongly modulated response of periodic cycles of attenuation and growing vibration amplitude. During each cycle, the prism vibration amplitude grows to reach a maximum value of 30 mm, then decreases sharply due to ball rotation. The vibrating prism transfers energy to the NES in the form of kinetic energy resulting in high

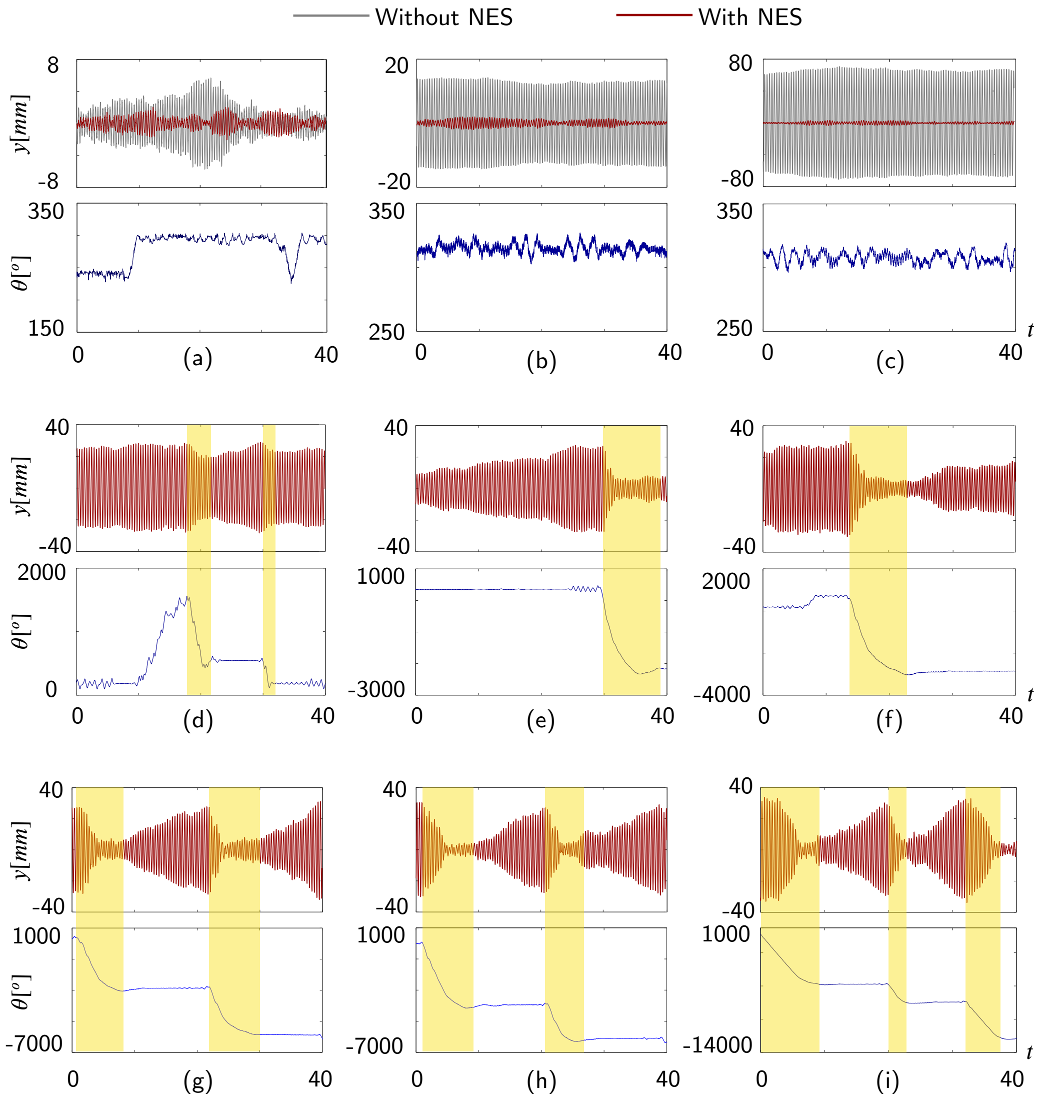

Figure 7: Time histories $y(t)$ of the prism displacement equipped with a NES (red curve) and NES ball angular displacement $\theta(t)$ in degrees (blue curve) measured at different flow speeds U =: (a) 9.0 m/s; (b) 9.7 m/s; (c) 11.2 m/s; (d) 12.7 m/s; (e) 14.2 m/s; (f) 15.7 m/s; (g) 17.2 m/s; (h) 18.7 m/s; and (i) 20.2 m/s. Dynamics of the prism without NES (gray curve) is shown only in (a)-(c).

angular speeds of the rotating ball. The ball rotation and the consequent energy dissipation through the TET mechanism drastically mitigate the prism galloping amplitude to less than 0.1 mm. From Figs. 7 (e-i), we can also observe that the frequency of the repeated periodic cycles of the reducing and growing amplitudes increases at higher flow speed. The strongly modulated response of the vibrating prism observed experimentally in the rotational regime is similar to that previously predicted by Tumkur et al. (2017), and demonstrates the energy transfer between the prism and the rotative NES during its galloping.

At large reduced velocities, beyond the rotational regime, the NES is ineffective and the galloping amplitude is above the limits of our experimental setup. We can say that the amount of energy extracted by the vibrating prism from the airflow exceeds the energy dissipation rate of the NES. Another hypothesis is that the inertial coupling between the NES and the prism is no longer beneficial at large amplitudes. Testing these hypotheses should be part of future work.

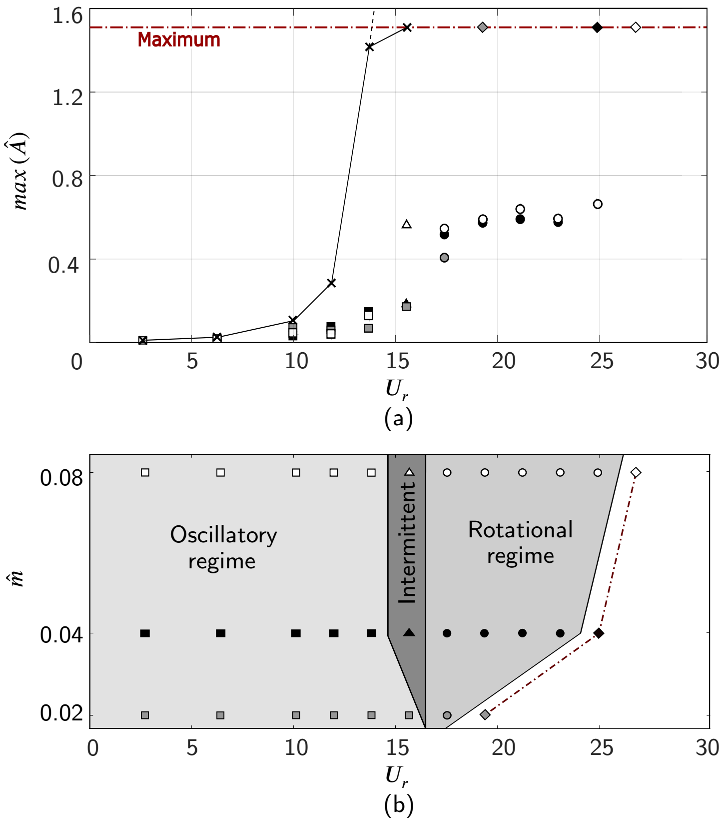

Figure 8: (a) Prism responses without ✕ and with a NES of mass ratio $\hat{m} = 0.02$ (black marks), $\hat{m} = 0.04$ (gray marks), and $\hat{m} = 0.08$ (white marks) at a constant $\hat{r} = 0.6$, (b) NES regimes mapping presenting oscillatory □, Intermittent △, and Rotational ○ regimes, and the points that reach the maximum allowed amplitude ◇ .

3.3. Influence of main NES parameters

We explore the influence of each of the main NES parameters individually. The modular NES design presented in section 2.2 allows easy modification of the main parameters. Depending on the ball mass, the mass ratio $\hat{m}$ can be varied between 0.02 and 0.08. Bushings of different sizes allow varying the NES radius ratio $\hat{r}$ (from 0.4 to 0.7) and the NES track relative clearance $\hat{\mu}$ (from 0.066 to 0.33). We reduce the ball friction with the NES track by adding a lubricating fluid to investigate the effect of the friction.

We compare the prism response with various NES configurations and define NES regimes based on the difference between the non-dimensional maximum and minimum vibration amplitudes. This difference is variable across the different regimes: a large value in the rotational regime and a small one in the oscillatory regime. We developed a MATLAB code to automatically categorizes the NES regimes depending on this difference and plot a NES regime mapping for each configuration of parameters based on the following criterion:

$$\begin{array}{rlcl} \text{if} & max(\hat{A}) - min(\hat{A}) > 0.2 & \Rightarrow & \text{rotational regime,} \\ \text{else if} & max(\hat{A}) - min(\hat{A}) > 0.1 & \Rightarrow & \text{intermittent regime,} \\ \text{else} & & \Rightarrow & \text{oscillatory regime.} \end{array}$$

3.3.1. Mass ratio $\hat{m}$

Fig. 8(a) presents the non-dimensional maximum amplitude $\hat{A}$ *versus* the reduced flow velocities U_r for the prism with NES configurations with different mass ratios $\hat{m}$ of 0.02, 0.04, and 0.08, considering a constant radius ratio $\hat{r} =$ 0.6 and a relative radial clearance $\hat{\mu} = 0.066$. The NES of the smallest mass ratio $\hat{m} = 0.02$ reduces the maximum amplitude in a small range of flow speeds $U_r \leq 19.2$. For mass ratios $\hat{m} = 0.04$ and 0.08, the prism maximum amplitude increases steadily with flow speeds until reduced flow velocities of 15.6 and 13.7, respectively. Then, it jumps at higher

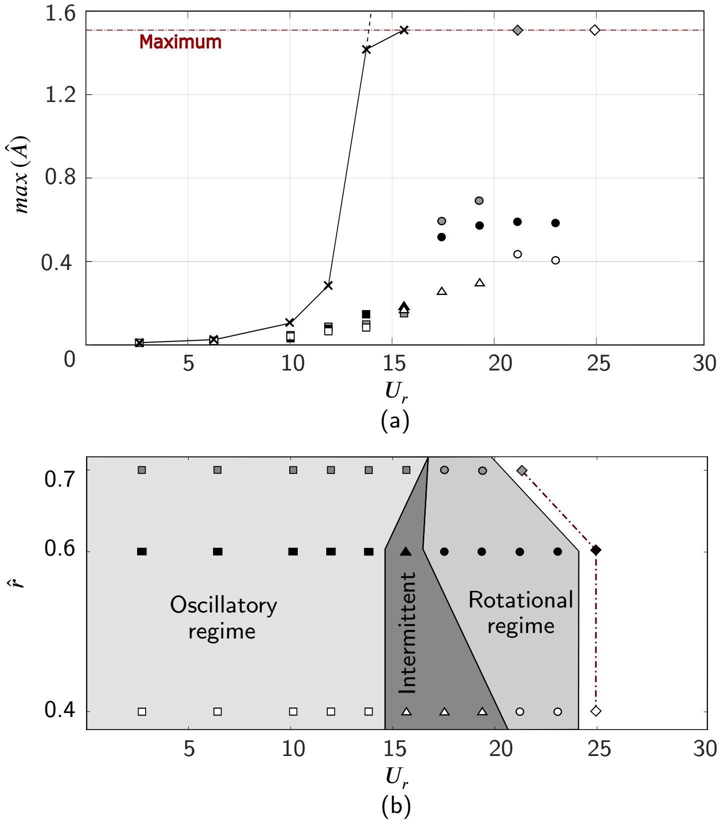

Figure 9: (a) Prism responses without ⇸ and with a NES of radius ratio $\hat{r} = 0.4$ (black marks), $\hat{r} = 0.6$ (gray marks), and $\hat{r} = 0.7$ (white marks) at a constant $\hat{m} = 0.04$, (b) NES regimes mapping presenting oscillatory □, Intermittent △, and Rotational ○ regimes, and the points that reach the maximum allowed amplitude ◇ .

flow speed coinciding with the NES transition from the oscillatory to the intermittent regime and continues with slight changes until another higher jump exceeding the limit of the experiment at reduced flow velocities $U_r = 25$ and 27, respectively. This means that increasing the NES mass ratio expands the NES effective range. However, lower mass ratio NES configurations result in smaller vibration amplitudes in the low-speed range.

Fig. 8(b) shows a NES regime mapping for the three different mass ratios. The oscillatory regime ends at a reduced flow velocity between 14.7 and 16.5 for both mass ratios 0.04 and 0.08. The intermittent regime starts and remains only for a small range of velocities until $U_r = 16.5$. While for the smallest mass ratio, $\hat{m} = 0.02$, the oscillatory regime range expands to eliminate the occurrence of the intermittent regime. For the three different mass ratios, the rotational regime starts at the same reduced velocity of 16.5 until reaching the maximum allowed amplitude.

3.3.2. Radius ratio $\hat{r}$

The behaviour of the NES is greatly affected by the NES radius ratio. A ball of 56 g mass and 24 mm diameter is used to obtain three different radius ratios $\hat{r} = 0.4$, 0.6 and 0.7, considering a constant mass ratio $\hat{m} = 0.04$ and relative radial clearance $\hat{\mu} = 0.066$. Fig. 9(a) compares the prism responses with the three different NES configurations. The prism with the smaller radius ratio NES oscillates with lower amplitude. The NES effective range at a radius ratio $\hat{r} = 0.7$ is smaller than that at lower radius ratios of 0.4 and 0.6. Thus, increasing the NES radius ratio results in increasing the prism vibration amplitudes and decreasing the NES effective range.

The NES regime mapping in Fig. 9(b) shows the effect of NES radius ratio variation on the ball behaviour. The oscillating regime range is the same for both radius ratios 0.4 and 0.6 and expands to eliminate the occurrence of the intermittent regime at the radius ratio of 0.7. The intermittent regime is observed from a reduced velocity $U_r = 14.7$ and ends at reduced velocities of 20.3 and 16.5 for NES configurations with radius ratios 0.4 and 0.6, respectively. For

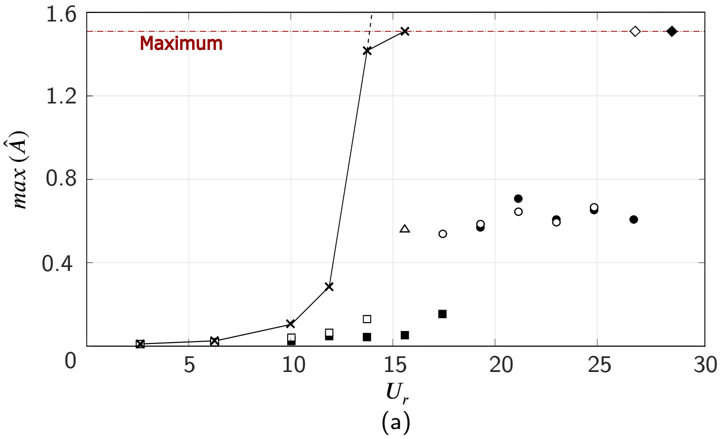

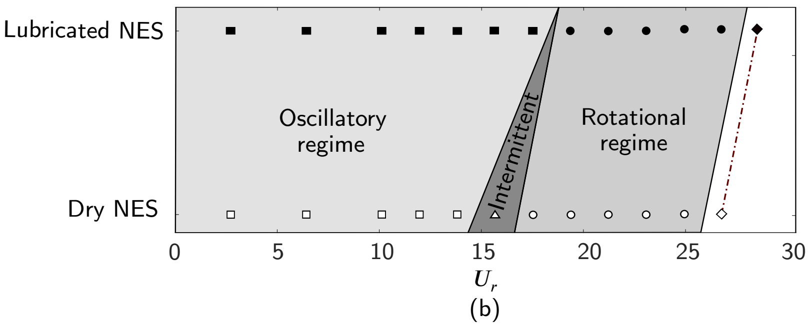

Figure 10: (a) Prism responses without —×— and with a dry (black marks) and lubricated (white marks) NESs with the same mass and radius ratios $\hat{m} = 0.08$, $\hat{r} = 0.6$, (b) NES regimes mapping presenting oscillatory □, Intermittent △, and Rotational ○ regimes, and the points that reach the maximum allowed amplitude ◇.

the highest value of radius ratio $\hat{r} = 0.7$, the rotational regime starts directly after the oscillatory regime at a reduced velocity of 16.5. The starting reduced velocities of the rotational regime are 20.3, 16.5, and 16.5 at the different radius ratios of 0.4, 0.6 and 0.7, respectively. Hence, increasing the NES radius ratio has a significant effect in narrowing the intermittent regime range.

3.3.3. Ball friction

The ball damping ratio ζ_θ has an important effect on the NES behaviour. Ball damping comes predominantly from the friction between the ball and the NES track. It is difficult to get an exact value for the ball damping ratio as it depends on uncertain parameters such as air resistance, and the ball behaviour (rolling or slipping). We added lubricating oil to reduce the ball friction with the NES track walls. We tested a lubricated and a dry NESs with the same parameters $\hat{m} = 0.08$, $\hat{r} = 0.6$ and $\hat{\mu} = 0.066$ to investigate the effect of ball damping variation.

The prism responses with the two NES configurations are presented in Fig. 10(a). The lubricated NES is more effective than the dry one in reducing the galloping amplitudes of the prism at the reduced flow velocities $13.6 < U_r < 17.4$. Fig. 10(b) shows the NES regime mapping for both the lubricated and the dry NES. The oscillatory regime range expands in the case of the lubricated NES to eliminate the appearance of the intermittent regime. While the rotational regime range is delayed by the lubricating fluid to start at a reduced velocity $U_r = 19.3$ instead of 17.4. A possible explanation for this finding is that the ball can rotate with higher angular speeds and absorb more energy from the system in the presence of lubrication due to decreased friction.

3.3.4. NES track relative clearance $\hat{\mu}$

Increasing the radial clearance $\hat{\mu}$ affects the ball rotation and increases the magnitude of the impacts between the ball and the NES track walls leading to different dynamics. Changing the inner bushing size allows achieving three

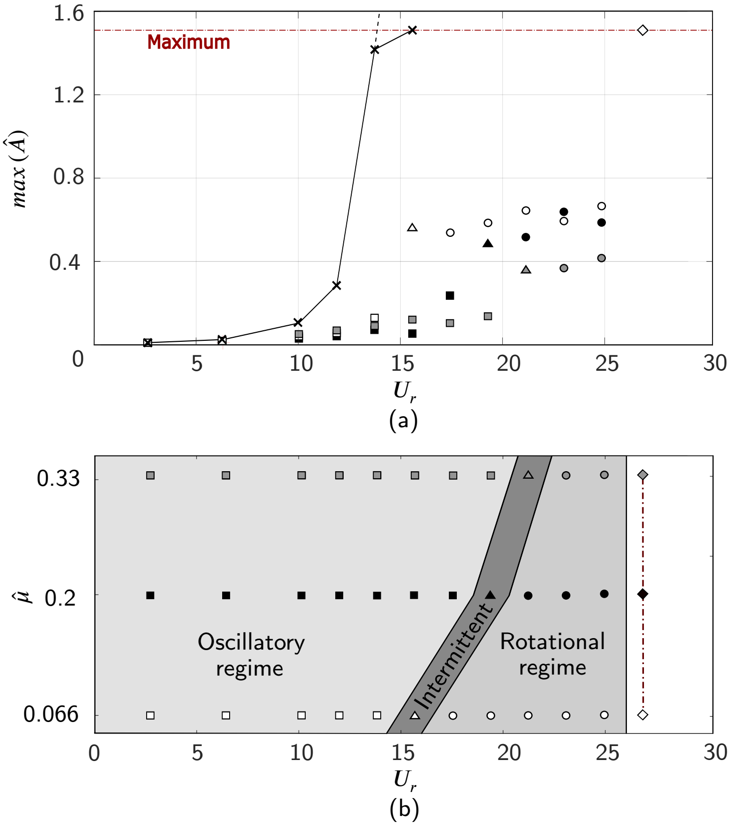

Figure 11: (a) Prism responses without ─×─ and with NESs of varying track relative clearance; $\hat{\mu} = 0.066$ (black marks), $\hat{\mu} = 0.2$ (gray marks), and $\hat{\mu} = 0.33$ (white marks) at a constant mass and radius ratios $\hat{m} = 0.08$, $\hat{r} = 0.66 \pm 0.01$, (b) NES regimes mapping presenting oscillatory □, Intermittent △, and Rotational ○ regimes, and the points that reach the maximum allowed amplitude ◇ .

relative NES track clearance values of 0.066, 0.2, and 0.33 for the same NES of mass ratio $\hat{m} = 0.08$ and radius ratio $\hat{r} = 0.61 \pm 0.01$.

The NES responses, presented in Fig. 11(a), are highly affected by the radial clearance. Increasing the radial clearance reduces the prism galloping amplitude, however, it does not change the NES effective range. Fig. 11(b) presents the NES regime mapping for the three different radial clearances. Increasing the radial clearance widens the oscillatory regime range and shifts the intermittent regime with no change in its range. We observe the oscillatory regime up to reduced flow velocities of 14.7, 18.3, and 20.2 at different radial clearances of 1, 3, and 5 mm, respectively. The findings at higher radial clearance may be explained by the effect of the ball impact with the NES track walls that appear as an additional way for nonlinear energy absorption.

4. Conclusion

The typical form of a rotative NES presented in the literature consists of a tip mass coupled to a primary structure by a rigid bar of fixed length. In this research, we designed a new rotative NES using a free metal ball moving in a circular track without direct coupling to the primary system proposing a simple, robust and effective way of nonlinear energy absorption. At least to the authors' knowledge, experimental investigation focusing on the galloping suppression using NES is not found in the literature and is the major novelty of this paper.

The rotative NES proposed in this study successfully mitigates the galloping of a square prism with no effect on its natural frequency. Wind tunnel experiments exposed the mechanism of action of the proposed NES and highlighted its three different response modes: oscillatory regime, intermittent regime, and rotational regime. At low flow speeds in the oscillatory regime, the NES ball oscillates with a small amplitude not exceeding 70 degrees, however, it increases the critical galloping velocity. At higher flow speeds, the intermittent regime appears within a small flow speed range. The ball oscillates with relatively low angular speeds to keep the prism amplitude less than 30 mm resulting in a nearly steady vibration of the prism. At higher flow speeds still, the rotational regime shows the maximum reduction for the prism vibration, where the NES ball rotates with high angular speeds and absorbs a high amount of energy. The ball rotation directly reduces the prism vibrations resulting in periodic cycles of reduction and growing in the prism vibration displacement.

The design of the NES allows for easy changes of its main parameters by swapping some components. Capitalising on this advantage, we experimentally quantified the influence of the main NES parameters on both the prism galloping response and the NES regime mapping over flow velocities. Increasing the mass ratio increases the NES effective range, and leads to the appearance of the intermittent regime coinciding with a small jump in the prism amplitude response. On the contrary, increasing the radius ratio decreases the NES effective range, and reduces the intermittent regime range rising the prism vibration amplitudes. Decreasing the ball friction with the NES track increases the NES effective range, and reduces the intermittent regime range. Hence, it eliminates the small jump in prism amplitude coinciding with the starting of the intermittent regime. We highlight the clearance between the NES track walls and the rotating ball as an effective parameter. Increasing the radial clearance significantly reduces the prism vibration amplitudes. For the range of parameter values considered here, the most efficient NES possess the highest mass ratio and radial clearance, and the lowest radius ratio.

The simple structure of the presented NES may extend its usage to many applications. It can damp wind-induced galloping on different types of structures such as power lines, high mounted signboards, long slender structures and skyscrapers. Our experiments are limited to a maximum non-dimensional amplitude of 1.5. Consequently, an accurate numerical model is important in future work to predict the NES behaviour and prism dynamics at high vibration amplitudes. These mathematical models are under development.

Acknowledgements

We acknowledge the Military Technical College (MTC) in Egypt and the Natural Sciences and Engineering Research Council of Canada (NSERC) for sponsoring the current project. The second author acknowledges the Fonds de Recherche du Québec – Nature et technologies (FRQNT) for sponsoring his short-term period (from December/ 2017 to February/ 2018) as a visiting researcher at Polytechnique Montreal. We want to thank Alexandre Medeiros, and Constant Roussel for their work in developing the experimental setup, as well as Sima Rishmawi for her help in image processing. We are also grateful for the insightful comments offered by Raed Bouslama.

References

AL-Shudeifat, M.A., Wierschem, N., Quinn, D.D., Vakakis, A.F., Bergman, L.A., Spencer, B.F., 2013. Numerical and experimental investigation of a highly effective single-sided vibro-impact non-linear energy sink for shock mitigation. International Journal of Non-Linear Mechanics 52, 96–109.

Bearman, P., Gartshore, I., Maull, D., Parkinson, G.V., 1987. Experiments on flow-induced vibration of a square-section cylinder. Journal of Fluids and Structures 1.

Blanchard, A., Bergman, L.A., Vakakis, A.F., 2020. Vortex-induced vibration of a linearly sprung cylinder with an internal rotational nonlinear energy sink in turbulent flow. Nonlinear Dynamics 99, 593–609.

Chen, H.W., Zhang, Q.J., Wu, X.Q., 2015. Stability and dynamic analyses of a horizontal axis washing machine with a ball balancer. Mechanism and Machine Theory 87, 131–149.

Dai, H.L., Abdelkefi, A., Wang, L., 2016. Usefulness of passive non-linear energy sinks in controlling galloping vibrations. International Journal of Non-Linear Mechanics 81, 83–94.

Dai, H.L., Abdelkefi, A., Wang, L., 2017. Vortex-induced vibrations mitigation through a nonlinear energy sink. Communications in Nonlinear Science and Numerical Simulation 42, 22–36.

Dongyang, C., Abbas, L.K., Guoping, W., Xiaoting, R., Marzocca, P., 2018. Numerical study of flow-induced vibrations of cylinders under the action of nonlinear energy sinks (NESs). Nonlinear Dynamics 94, 925–957.

Gendelman, O.V., 2008. Targeted energy transfer in systems with non-polynomial non linearity. Journal of Sound and Vibration 315, 732–745.

Gendelman, O.V., Alloni, A., 2015. Dynamics of forced system with vibro-impact energy sink. Journal of Sound and Vibration 358, 301–314.

Guo, H., Liu, B., Yu, Y., Cao, S., Chen, Y., 2017. Galloping suppression of a suspended cable with wind loading by a nonlinear energy sink. Archive of Applied Mechanics 87, 1007–1018.

Hijmissen, J.W., van Horssen, W.T., 2007. On aspects of damping for a vertical beam with a tuned mass damper at the top. Nonlinear Dynamics 50, 169–190.

Lee, Y.S., Vakakis, A.F., Bergman, L.A., McFarland, D.M., Kerschen, G., Nucera, F., Tsakirtzis, S., Panagopoulos, P.N., 2008. Passive non-linear targeted energy transfer and its applications to vibration absorption: A review. Proceedings of the Institution of Mechanical Engineers, Part K: Journal of Multi-body Dynamics 222, 77–134.

Li, T., Lamarque, C., Seguy, S., Berlioz, A., 2018. Chaotic characteristic of a linear oscillator coupled with vibro-impact nonlinear energy sink. Nonlinear Dynamics 91, 2319–2330.

Lu, C.J., Hung, C.H., 2008. Stability analysis of a three-ball automatic balancer. Journal of Vibration and Acoustics 130.

Majewski, T., Szwedowicz, D., Melo, M.A.M., 2015. Self-balancing system of the disk on an elastic shaft. Journal of Sound and Vibration 359, 2–20.

Makram, M., Kossa, S.S., Khalil, M.K., Nemnem, A.F., Samer, G., 2017. Experimental investigation of ABB effect on unbalanced rotor vibration. Journal of Coupled Systems and Multiscale Dynamics 7, 225–231.

Mehmood, A., Nayfeh, A.H., Hajj, M.R., 2014. Effects of a non-linear energy sink (NES) on vortex-induced vibrations of a circular cylinder. Nonlinear Dynamics 77, 667–680.

Pennisi, G., Stephan, C., Gourc, E., Michon, G., 2017. Experimental investigation and analytical description of a vibro-impact NES coupled to a single-degree-of-freedom linear oscillator harmonically forced. Nonlinear Dynamics 88, 1769–1784.

Saeed, A.S., AL-Shudeifat, M.A., Vakakis, A.F., 2019. Rotary-oscillatory nonlinear energy sink of robust performance. International Journal of Non-Linear Mechanics 117, 103249.

Teixeira, B., Franzini, G.R., Gosselin, F., 2018. Passive suppression of transverse galloping using a nonlinear energy sink. Proceeding of the 9^{th} International Symposium on Fluid-Structure Interactions, Flow-Sound Interactions, Flow-Induced Vibration and Noise .

Tumkur, R.K.R., Domany, E., Gendelman, O.V., Masud, A., Bergman, L.A., Vakakis, A.F., 2013. Reduced-order model for laminar vortex-induced vibration of a rigid circular cylinder with an internal nonlinear absorber. Communications in Nonlinear Science and Numerical Simulation 18, 1916–1930.

Tumkur, R.K.R., Pearlstein, A.J., Masud, A., Gendelman, O.V., Blanchard, A.B., Bergman, L.A., Vakakis, A.F., 2017. Effect of an internal nonlinear rotational dissipative element on vortex shedding and vortex-induced vibration of a sprung circular cylinder. Journal of Fluid Mechanics 828, 196–235.

Ueno, T., Franzini, G.R., 2019. Numerical studies on passive suppression of one and two degrees-of-freedom vortex-induced vibrations using a rotative non-linear vibration absorber. International Journal of Non-Linear Mechanics 116, 230–249.

Vakakis, A.F., Gendelman, O.V., Bergman, L.A., McFarland, D.M., Kerschen, G., Lee, Y.S., 2008. Nonlinear targeted energy transfer in mechanical and structural systems. volume 156. Springer Science & Business Media.

Wang, J., Wierschem, N., Spencer, B.F., Lu, X., 2016. Numerical and experimental study of the performance of a single-sided vibro-impact track nonlinear energy sink. Earthquake Engineering & Structural Dynamics 45, 635–652.

Wierschem, N.E., Hubbard, S.A., Luo, J., Fahnestock, L.A., Spencer, B.F., McFarland, D.M., Quinn, D.D., Vakakis, A.F., Bergman, L.A., 2017. Response attenuation in a large-scale structure subjected to blast excitation utilizing a system of essentially nonlinear vibration absorbers. Journal of Sound and Vibration 389, 52–72.

Wierschem, N.E., Quinn, D.D., Hubbard, S.A., Al-Shudeifat, M.A., McFarland, D.M., Luo, J., Fahnestock, L.A., Spencer, B.F., Vakakis, A.F., Bergman, L.A., 2012. Passive damping enhancement of a two-degree-of-freedom system through a strongly nonlinear two-degree-of-freedom attachment. Journal of Sound and Vibration 331, 5393–5407.